



Numerical investigation on the effect of tumor on the thermal behavior inside the skin tissue



Zhuo-Jia Fu^{a,b,*}, Qiang Xi^{a,b}, Leevan Ling^{c,*}, Chang-Yong Cao^d

^aCenter for Numerical Simulation Software in Engineering & Sciences, College of Mechanics and Materials, Hohai University, Nanjing, Jiangsu 210098, China

^bState Key Laboratory of Acoustics, Institute of Acoustics, Chinese Academy of Sciences, Beijing 100190, China

^cDepartment of Mathematics, Hong Kong Baptist University, Kowloon Tong, Hong Kong

^dDepartment of Mechanical Engineering & Materials Science, Duke University, Durham, NC 27708, USA

ARTICLE INFO

Article history:

Received 7 July 2016

Received in revised form 7 October 2016

Accepted 13 November 2016

Available online 9 January 2017

Keywords:

Meshless method

Method of approximate particular solution

Affine space decomposition

Thermal behavior

Pennes bioheat equation

ABSTRACT

This paper investigates the thermal behavior inside skin tissue with the presence of a tumor by solving the Pennes bioheat equation. We apply the method of approximate particular solutions (MAPS) to simulate tumor in 3D. The MAPS is a kind of domain-type meshless collocation methods, which has the merits being free of mesh generation and numerical integration. To ensure the interface conditions were exactly satisfied, an affine space decomposition technique is adopted. After verifying the convergence of the proposed method, we provide various simulations to the thermal effects inside the skin tissue due to an arbitrary-shaped tumor, including the location, geometry and size.

Published by Elsevier Ltd.

1. Introduction

The presence of a tumor inside healthy skin tissues makes the temperature nearby increases [1–3]. This anomalous thermal behavior is caused by the relatively higher metabolic heat and blood perfusion of the tumor in comparison with healthy tissues. By comparing the thermograms of normal and infected tissues, such thermal property can be used to detect tumor under the skin tissues.

The well-known Pennes equation [4], which involves the effects of blood perfusion and metabolic heat generation, is a commonly-used model for simulating the thermal behavior of skin tissue. Let u_T and u_S be the temperature in the tumor and surrounding tissue respectively. With the presence of a tumor, both temperature distributions can be modeled by a diffusion-reaction equation:

$$\rho c \frac{\partial}{\partial t} u(\mathbf{x}, t) = \nabla \cdot (k \nabla u(\mathbf{x}, t)) + \omega_b \rho_b c_b (u_a - u(\mathbf{x}, t)) + Q, \mathbf{x} \in \Omega, t \in (0, T). \quad (1)$$

where k , ρ , c denote the constant thermal conductivity, density and specific heat of the skin tissue, respectively. The parameters ω_b , ρ_b , c_b denote the perfusion rate, density and specific heat of the blood,

* Corresponding authors at: Center for Numerical Simulation Software in Engineering & Sciences, College of Mechanics and Materials, Hohai University, Nanjing, Jiangsu 210098, China (Z.-J. Fu and L. Ling).

E-mail addresses: paul212063@hhu.edu.cn (Z.-J. Fu), lling@hkbu.edu.hk (L. Ling).

respectively. The other constants, u_a , Q are the arterial temperature and metabolic heat generation, which are all known quantities.

We are interested in solving the PDE in (1) in some truncated domains $\Omega = \Omega_T \cup \Omega_S$ that include the tumor in Ω_T with sufficient surrounding of healthy tissue in Ω_S with $\Omega_T \cap \Omega_S = \emptyset$. Fig. 1 gives a schematic demonstration of such computational domains. Let u_T and u_S denote the temperature in the tumor region Ω_T and the healthy tissue region Ω_S , respectively. On the skin/tumor interface, both temperature and heat flux remain continuous. Hence, the interface conditions $\Gamma_I = \overline{\Omega_T} \cap \overline{\Omega_S}$ that connect the temperature profiles in the two regions are:

$$\begin{aligned} u_T(\mathbf{x}, t) &= u_S(\mathbf{x}, t), \quad \mathbf{x} \in \Gamma_I, t \in (0, T], \\ \frac{\partial}{\partial n} u_T(\mathbf{x}, t) + \frac{\partial}{\partial n} u_S(\mathbf{x}, t) &= 0, \quad \mathbf{x} \in \Gamma_I, t \in (0, T]. \end{aligned} \quad (2)$$

Consider the whole surface of the truncated domain. On the interior surface facing the body core Γ_1 , we simply impose the Dirichlet boundary condition,

$$u_S(\mathbf{x}, t) = u_a, \quad \mathbf{x} \in \Gamma_1, t \in (0, T]. \quad (3)$$

We assume the remaining surface of the truncated domain Γ_2 is insulated to guarantee the continuity of numerical solutions inside and outside the truncated domain. In practice, the skin surface is covered with an insulating material large enough to guarantee the temperature inside the body to reach the steady state and to avoid the effect from the surrounding environment, namely, we impose the Neumann boundary condition

Nomenclature

$(\cdot)^{(n)}$	variable at time level n	A	known matrix in (17)
$(\cdot)^{(n+1)}$	variable at time level $n + 1$	B	known matrix in (17)
$(\cdot)_\chi$	variable in the truncated domain	B^\dagger	pseudoinverse matrix of B
$(\cdot)_S$	variable in health skin tissue domain	C	parameter in (19)
$(\cdot)_T$	variable in tumor domain	c	specific heat of tissue
α	unknown coefficients in (12)	c_b	specific heat of blood
$\boldsymbol{\alpha}$	unknown coefficient vector in (14)	c_{MQ}	MQ-RBF shape parameter
ξ	RBF centers	f	known vector in (17)
$\boldsymbol{\beta}$	unknown coefficients in (18)	G	right handed data generator
\mathcal{B}	boundary condition operators	g	known vector in (17)
\mathcal{L}_χ	modified Helmholtz operators	h	initial boundary conditions
\mathcal{N}	null matrix of B	k	thermal conductivity of tissue
Γ_I	interface boundary	M	number of RBF centers
Γ_1	Dirichlet boundary of the truncated domain	N	number of collocation nodes
Γ_2	Neumann boundary of the truncated domain	p	parameter in derived RBFs
λ	parameter in modified Helmholtz operator	Q	metabolic heat generation
Λ_χ	linear operators	r_j	euclidean distance between collocation nodes and RBF centers
\mathbf{x}	collocation nodes	T	time instant in Steady-state situation
Ω	truncated domain	u	temperature
ω_b	perfusion rate of blood	u_0	initial temperature
Ω_S	health skin tissue domain	u_a	arterial temperature
Ω_T	tumor domain	X	collocation node set
Φ	derived RBFs	x	normal direction of the skin surface
ϕ	RBFs	y	one orthogonal direction tangent to the skin surface
ρ	density of tissue	z	the other one orthogonal direction tangent to the skin surface
ρ_b	density of blood		
τ	time stepping size		
Ξ	RBF center set		

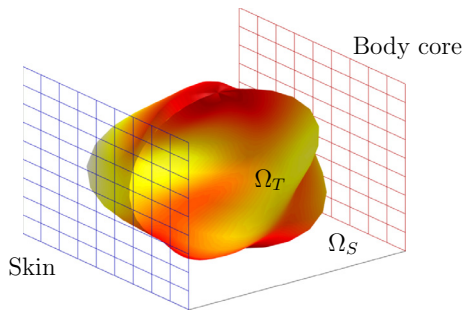


Fig. 1. Schematic diagram of a tumor in Ω_T embedded in healthy skin tissues Ω_S .

$$\frac{\partial}{\partial n} u_S(\mathbf{x}, t) = 0, \quad \mathbf{x} \in \Gamma_2, \quad t \in (0, T]. \quad (4)$$

on both the artificial and skin surfaces. Along with initial conditions,

$$\begin{cases} u_T(\mathbf{x}, 0) = h_T(\mathbf{x}), & \mathbf{x} \in \Omega_T, \\ u_S(\mathbf{x}, 0) = h_S(\mathbf{x}), & \mathbf{x} \in \Omega_S. \end{cases} \quad (5)$$

Various numerical methods for solving the above-mentioned Pennes Eqs. (1)–(5) can be found in the literature. For example, pseudospectral collocation Chebyshev method [5] for convective boundary conditions, spectral element method [6] for Pennes bioheat transfer, meshless radial basis function collocation method [7] for heterogeneous heat conduction. However, most of the above-mentioned researches only consider 2D skin tissues with regular tumor. The effect of the arbitrary-shaped tumor on the thermal behavior inside the skin tissue remains unexplored. This paper focuses on numerical method for solving a 3D Pennes bioheat equation. To solve this time independent equation with different materials in multi-connected regions, in Section 2, we propose using the method of approximate particular solutions (MAPS) [8,9] to solve the corresponding semi-discretized equation. In order

to guarantee the numerical stability and accuracy in interface condition, an affine space decomposition technique [10] is included in our numerical implementation. In Section 3, numerical verifications are given to demonstrate the effectiveness of the proposed method. Then, we simulate the thermal effects of different arbitrary-shaped tumors inside the skin tissue. Finally, in Section 4, we shall draw some conclusions based on the numerical simulations.

2. Method of approximate particular solutions and affine-decomposition

In this section, we propose a numerical method to solve the Pennes bioheat equation, as defined in (1)–(5), which can be treated as a PDE with piecewise constant coefficients; for $\chi = \{S, T\}$, we consider PDEs in the form of:

$$\frac{\partial}{\partial t} u_\chi(\mathbf{x}, t) = a_\chi \Delta u_\chi(\mathbf{x}, t) + b_\chi u_\chi(\mathbf{x}, t) + c_\chi, \quad \mathbf{x} \in \Omega_\chi, \quad t \in (0, T), \quad (6)$$

with the boundary conditions

$$\begin{cases} u_S(\mathbf{x}, t) = u_a, & \mathbf{x} \in \Gamma_1, \quad t \in (0, T), \\ \frac{\partial}{\partial n} u_S(\mathbf{x}, t) = 0, & \mathbf{x} \in \Gamma_2, \quad t \in (0, T), \end{cases} \quad (7)$$

with the interface boundary conditions

$$\begin{cases} u_S(\mathbf{x}, t) = u_T(\mathbf{x}, t), & \mathbf{x} \in \Gamma_I, \quad t \in (0, T), \\ \frac{\partial}{\partial n} u_S(\mathbf{x}, t) + \frac{\partial}{\partial n} u_T(\mathbf{x}, t) = 0, & \mathbf{x} \in \Gamma_I, \quad t \in (0, T), \end{cases} \quad (8)$$

with the initial conditions

$$u_\chi(\mathbf{x}, 0) = h_\chi(\mathbf{x}), \quad \mathbf{x} \in \Omega_\chi, \quad (9)$$

where $a_\chi = \frac{k_\chi}{\rho c}$, $b_\chi = \frac{-\omega_b \rho_b c_b}{\rho c}$, $c_\chi = \frac{\omega_b \rho_b c_b u_a + Q}{\rho c}$, and $\Omega_S \cap \Omega_T = \emptyset$ and $\Omega_S \cup \Omega_T = \Omega$ in these generalized notations. Their boundaries $\partial\Omega_S = \Gamma_1 \cup \Gamma_2 \cup \Gamma_I$ and $\partial\Omega_T = \Gamma_I$.

Our study focuses on a semi-discretized form of (6)–(9), which can be obtained by some temporal discretization; for example, by the implicit time-stepping scheme (backward Euler formulation), we can reduce the governing equation in (6) to

$$\mathcal{L}_\chi u_\chi^{(n+1)}(\mathbf{x}) = \Lambda_\chi(\tau, u_\chi^{(n)}(\mathbf{x})) \quad \text{for } \mathbf{x} \in \Omega_\chi, \tag{10}$$

for the modified Helmholtz operators $\mathcal{L}_\chi = \Delta - \lambda^2$ for $\chi = \{S, T\}$, where $\lambda = \sqrt{\frac{1}{a_\chi \tau} - \frac{b_\chi}{a_\chi}}$ whose coefficients depend on the parameter in (6) and discrete time $\tau \in \{t_1, t_2, \dots, T\}$, that relate the solutions at times t_n . The right handed function can be computed by the linear operator $\Lambda_\chi(\tau, u_\chi^{(n)}(\mathbf{x})) = -\frac{u_\chi^{(n)}(\mathbf{x})}{a_\chi \tau} - \frac{c_\chi}{a_\chi}$ using the solution in the previous time step. Other higher order discretization is possible and the resultant elliptic semi-discretized equation can be solved similarly by the proposed method. The boundary/interface conditions can also be simplified to

$$\begin{aligned} \mathcal{B}_{\Gamma_1 \cup \Gamma_2} u_S^{(n+1)}(\mathbf{x}) &= G_{\Gamma_1 \cup \Gamma_2}(u_S^{(n)}(\mathbf{x}), u_T^{(n)}(\mathbf{x})), \quad \mathbf{x} \in \Gamma_1 \cup \Gamma_2, \\ \mathcal{B}_{\Gamma_I} u_\chi^{(n+1)}(\mathbf{x}) &= G_{\Gamma_I}(u_S^{(n)}(\mathbf{x}), u_T^{(n)}(\mathbf{x})), \quad \mathbf{x} \in \Gamma_I, \end{aligned} \tag{11}$$

where \mathcal{B} is defined piecewise, either of Dirichlet or Neumann type, depending on the location of \mathbf{x} , and similarly to the right handed data generator G .

To solve the semi-discretized equation in (10) numerically, we employ the MAPS, proposed by Chen et al. [9]. Over the past years, the MAPS has been successfully applied to various physical and engineering problems, such as anisotropic problems [11], nonhomogeneous Cauchy problems [12], wave problems [13], elasticity problems [14], Navier-Stokes equation [15], convection-diffusion problems [16] and fractional diffusion problems [17]. In comparison with the well-known radial basis function (RBF) collocation methods, a.k.a. the Kansa method [18,19], the MAPS uses problem-dependent basis functions derived from the governing equation operator. Numerical evidence [20,21] suggested that the MAPS outperforms the Kansa method in terms of both the stability and accuracy, which is particularly obvious in the evaluation of partial derivatives of numerical solutions.

The MAPS, as one of the meshless collocation methods [22–24], can be set up by defining trial basis function and finding unknown coefficients by collocation. Since the domain of (6) is multi-regional, we will use two numerical expansions to approximate the temperature profiles in the healthy skin and tumor respectively. Let $U_\chi^{(n)}(\cdot)$ denotes the numerical approximation to $u_\chi(\cdot, t_n)$ in Ω_χ , and is expanded as a linear combination of M_χ basis functions $\Phi_\chi(r_j, \lambda)$ centered at $\Xi_\chi := \{\xi_1, \dots, \xi_{M_\chi}\} \subset \overline{\Omega}_\chi$:

$$U_\chi^{(n)}(\mathbf{x}) = \sum_{\xi_j \in \Xi_\chi} [\alpha_\chi^{(n)}]_j \Phi_\chi(r_j, \lambda) \text{ with } r_j = \|\mathbf{x} - \xi_j\|, \tag{12}$$

where $[\alpha_\chi^{(n)}]_j$ denotes the unknown coefficients. Instead of the commonly used basis functions (i.e., the multiquadrics and Gaussian), the MAPS uses trial basis functions in the form of

$$\Phi(r; \lambda) = -\sum_{j=0}^{p/2} \frac{(-1)^j p! r^{p-2j+1}}{(p-2j)! \lambda^{2j+2}} + \frac{p! e^{-\lambda r}}{\lambda^{p+2} r}, \tag{13}$$

that solves the modified Helmholtz $(\Delta - \lambda^2)\Phi(r; \lambda) = \phi(r)$ in \mathbb{R}^3 for different polynomial splines $\phi(r) = r^{p-1}$ for even p [25]. For $p = 8$, and 10, we have

$$\Phi(r; \lambda) = \begin{cases} -\frac{r^7}{\lambda^2} - \frac{56r^5}{\lambda^4} - \frac{1680r^3}{\lambda^6} - \frac{20160r}{\lambda^8} - \frac{40320}{\lambda^{10}r} + \frac{40320e^{-\lambda r}}{\lambda^{10}r}, & r \neq 0, \\ -\frac{40,320}{\lambda^9}, & r = 0, \end{cases}$$

and

$$\Phi(r; \lambda) = \begin{cases} -\frac{r^9}{\lambda^2} - \frac{90r^7}{\lambda^4} - \frac{5040r^5}{\lambda^6} - \frac{151200r^3}{\lambda^8} - \frac{1814400r}{\lambda^{10}} - \frac{3,628,800}{\lambda^{12}r} + \frac{3,628,800e^{-\lambda r}}{\lambda^{12}r}, & r \neq 0, \\ -\frac{3,628,800}{\lambda^{11}}, & r = 0, \end{cases}$$

respectively. Picking some parameters p allows us to complete the numerical expansion (12). Now, suppose we impose N_χ collocation conditions at some set $X_\chi \subset \overline{\Omega}_\chi$ respectively to spatially discretize the semi-discretized Eqs. (10) and (11). Then the resultant linear system can be expressed as

$$\begin{bmatrix} \mathcal{L}_S \Phi_S(X_S, \Xi_S) & \mathbf{0} \\ \mathbf{0} & \mathcal{L}_T \Phi_T(X_T, \Xi_T) \\ \mathcal{B}_{\Gamma_1} \Phi_S(X_S \cap \Gamma_1, \Xi_S) & \mathbf{0} \\ \mathcal{B}_{\Gamma_2} \Phi_S(X_S \cap \Gamma_2, \Xi_S) & \mathbf{0} \\ \mathcal{B}_{\Gamma_I} \Phi_S(X_S \cap \Gamma_I, \Xi_S) & -\mathcal{B}_{\Gamma_I} \Phi_T(X_S \cap \Gamma_I, \Xi_T) \\ \mathcal{B}_{\Gamma_I} \Phi_S(X_T \cap \Gamma_I, \Xi_S) & \mathcal{B}_{\Gamma_I} \Phi_T(X_T \cap \Gamma_I, \Xi_T) \end{bmatrix} \begin{bmatrix} \alpha_S^{(n+1)} \\ \alpha_T^{(n+1)} \end{bmatrix} = \begin{bmatrix} \Lambda_S \Phi_S(X_S, \Xi_S) \alpha_S^{(n)} \\ \Lambda_T \Phi_S(X_T, \Xi_T) \alpha_T^{(n)} \\ G_{\Gamma_1} \\ G_{\Gamma_2} \\ \mathbf{0} \\ \mathbf{0} \end{bmatrix}, \tag{14}$$

for solving unknown coefficients $\alpha_\chi^{(n+1)} \in \mathbb{R}^{M_\chi}$. By the solvability argument in [26] and the sake of numerical stability, we require the collocation points to be as dense as the trial RBF centers, i.e., $M_\chi \leq N_\chi$ for both $\chi = S$ and T , and the linear system in (14) is overdetermined. Implementing the standard least-squares approach to solve (14) will introduce error in the boundary and interface conditions. This leads to serious effects towards the accuracy of our simulations. To circumvent this problem, we adopt the affine space decomposition technique [10] and consider the following constraint least-squares problem:

$$\operatorname{argmin}_{\alpha_\chi \in \mathbb{R}^{M_\chi}} \left\| \begin{bmatrix} \mathcal{L}_S \Phi_S(X_S, \Xi_S) & \mathbf{0} \\ \mathbf{0} & \mathcal{L}_T \Phi_T(X_T, \Xi_T) \end{bmatrix} \begin{bmatrix} \alpha_S^{(n+1)} \\ \alpha_T^{(n+1)} \end{bmatrix} - \begin{bmatrix} \Lambda_S \Phi_S(X_S, \Xi_S) \alpha_S^{(n)} \\ \Lambda_T \Phi_S(X_T, \Xi_T) \alpha_T^{(n)} \end{bmatrix} \right\|_2, \tag{15}$$

subject to

$$\begin{bmatrix} \mathcal{B}_{\Gamma_1} \Phi_S(X_S \cap \Gamma_1, \Xi_S) & \mathbf{0} \\ \mathcal{B}_{\Gamma_2} \Phi_S(X_S \cap \Gamma_2, \Xi_S) & \mathbf{0} \\ \mathcal{B}_{\Gamma_I} \Phi_S(X_S \cap \Gamma_I, \Xi_S) & -\mathcal{B}_{\Gamma_I} \Phi_T(X_S \cap \Gamma_I, \Xi_T) \\ \mathcal{B}_{\Gamma_I} \Phi_S(X_T \cap \Gamma_I, \Xi_S) & \mathcal{B}_{\Gamma_I} \Phi_T(X_T \cap \Gamma_I, \Xi_T) \end{bmatrix} \begin{bmatrix} \alpha_S^{(n+1)} \\ \alpha_T^{(n+1)} \end{bmatrix} = \begin{bmatrix} G_{\Gamma_1} \\ G_{\Gamma_2} \\ \mathbf{0} \\ \mathbf{0} \end{bmatrix}, \tag{16}$$

For simplicity, we denote (15) and (16) as

$$\operatorname{argmin}_{\alpha \in \mathbb{R}^{M_S+M_T}} \|A\alpha - f\| \text{ subject to } B\alpha = g, \tag{17}$$

so that we enforce the discrete boundary and interface conditions exactly in the numerical solution. This minimization approach can also save us from searching the appropriate least-squares weighting [27] and yields robust numerical consistency.

To solve (17), we denote B^\dagger and \mathcal{N} as the pseudoinverse and the null matrix of B , that is, $B^\dagger B = I$ and $\mathcal{N}B = \mathbf{0}$, where I and $\mathbf{0}$ denote identity and zero matrices, respectively. Note that the matrix B in (17) is an underdetermined. As we expect that the domain-filling sets of $\Xi_S \cup \Xi_T$ contains a lot more points than the set of collocation points on the boundary and interface surfaces, the computational overhead for finding B^\dagger is reasonable. Using elementary arguments in linear algebra, we know that the unknown coefficients α will be in the form of

$$\alpha = B^\dagger g + \mathcal{N}\beta \tag{18}$$

for some new unknown coefficients β . We can work out the dimension of β in exact arithmetics. However, whenever B is not numerically of full rank, the affine decomposition approach can be seen as some sort of regularization, in which the computed null matrix

\mathcal{N} will contain extra columns to make up the missing rank. The extra degrees of freedom will be returned to the least-squares problem that is now posed on β as:

$$A(B^\dagger g + \mathcal{N}\beta) = f \text{ or } A\mathcal{N}\beta = f - AB^\dagger g.$$

Once we determine β , the original α can be found easily by (18). Using the numerical expansions in (12), the obtained numerical approximation can be evaluated anywhere in the domain Ω . Since all columns of \mathcal{N} is orthonormal, the length scale of the reduced matrix $A\mathcal{N}$ is completely determined by the governing operator. Note that the original matrix system (14) and the affine space approach (15) and (16) are mathematically different; the latter better matches with the physics in the considered bioheat problems. Numerical investigation shows that the affine decomposition approach is able to achieve better accuracy and more stable results than the direct solution of the original matrix.

3. Numerical simulations

In this section, we present four examples. In the first, we verify the performance of the proposed numerical approach by comparing the numerical solution to a steady-state problem. This example helps determining all the parameters for the rest of the simulations. In the second example, we compare our three-dimensional simulated results with the two-dimensional ones found in literature [28]. From this example, readers can clearly see the necessity of using three-dimensional models. These examples were performed on regular domains with structured grids so that the presented results can be easily reproduced. Then, the next two examples show the capability of meshless methods for irregular domains. In our third example, the effects of tumor's geometry on the resulting steady-state temperature distributions were studied. Lastly, we study the power of separation of the proposed scheme; that is, how far apart two tumors have to be so that the proposed method can tell them apart. In all simulations, typical parameters for skin tissue and tumor in Table 1 were employed, and let x be the normal direction of the surface, and y, z be any two orthogonal directions tangent to the surface. Moreover, the convergence criterion of time stepping process to the final steady-state situation $u_\chi(\mathbf{x}, T)$ is set as $|u_\chi^{(n+1)}(\mathbf{x}) - u_\chi^{(n)}(\mathbf{x})| \leq 10^{-3}$.

3.1. Example 1: Identifying parameters of numerical method

We consider a rectangular domain Ω_S as in Fig. 1 without the presence of tumors, i.e., $\Omega_T = \emptyset$. The skin surface and body core are located at $x=0$ and $x=0.03$ respectively, and $(y, z) \in [-0.04, 0.04] \times [-0.06, 0.06]$. In this simplified model, the skin and insulating surfaces Γ_2 are subjected to zero Neumann boundary conditions $\frac{\partial}{\partial n} u_S(\mathbf{x}, t) = 0$ whereas the body core Γ_1 has Dirichlet boundary condition $u_S(\mathbf{x}, t) = u_a$ for all $t \geq 0$. Then, the analytical steady-state temperature profile [29] is given by

$$u_S(\mathbf{x}, \infty) = 37 + \frac{Q}{\omega_b \rho_b c_b} \left(1 - \frac{e^{Cx} + e^{-Cx}}{e^{0.03C} + e^{-0.03C}} \right) \text{ for } \mathbf{x} \in \Omega_S, \quad (19)$$

Table 1
Typical skin tissue properties.

	Healthy tissue	Tumor
$\rho(\rho_b)$	1000 kg/m ³	1000 kg/m ³
$c(c_b)$	4000 J/(kg °C)	4000 J/(kg °C)
u_a	37 °C	37 °C
u_0	33 °C	33 °C
k	0.5 W/(m °C)	0.5 W/(m °C)
Q_S	420 W/m ³	4200 W/m ³
ω_b	0.0005 m ³ /s/m ³	0.002 m ³ /s/m ³

where $C = \sqrt{\omega_b \rho_b c_b / k}$.

In order to apply the proposed method in the previous section for solving (6)–(9) to steady-state situation, we need to identify a proper MAPS basis, i.e., by determining the parameter p in (13). Fig. 2 shows the L^∞ difference (measured on a very fine 29,791 evaluation nodes) between the analytical steady-state solution and our simulated solutions with different numbers of RBF center basis M in the present MAPS expansion (12), and various values of $p = 4, 6, 8,$ and $10,$ which are compared with the Kansa method using MQ-RBF ($\sqrt{(r_j/c_{MQ})^2 + 1}$), where the MQ-RBF shape parameters c_{MQ} for $M = 512, 729, 1000, 1331, 1728$ in this case are, respectively, 0.077, 0.061, 0.049, 0.039, 0.035 determined by using trial and error approach. Note that $p = 2$ does not yield smooth enough trial basis for the second order PDEs and is therefore excluded from the comparison. Although the Kansa method with optimal MQ-RBF shape parameter obtains the accurate results, it is a nontrivial task to determine the sensitive problem-dependent MQ-RBF shape parameter, which has the big effect on numerical accuracy. Moreover, it can be found from Fig. 2 that the numerical solutions obtained with $p = 4$ and 6 are still “converging” in the tested range of M . On the other hand, the maximum differences for the other two numerical solutions stagnate after $M = 1000$; hence, both $p = 8$ and 10 are suitable choices and we opt for the smaller value ($p = 8$) to avoid the problem of ill-conditioning.

Lastly, to ensure the proposed method is not sensitive to our selections, Table 2 shows more numerical results for $p = 8$ and $M = 1000$ with different temporal parameters T and τ . Hence we use $p = 8, M = 1000, T = 11000,$ and $\tau = 500$ for a balance between accuracy and efficiency in all numerical simulations throughout the section.

3.2. Example 2: Two- vs. three-dimensional simulations

Considers the same domain of skin tissue as in Example 1 but with a 0.01 thick rectangular tumor with surface size $0.02 \times z_T$ (perpendicular to the skin surface) given as

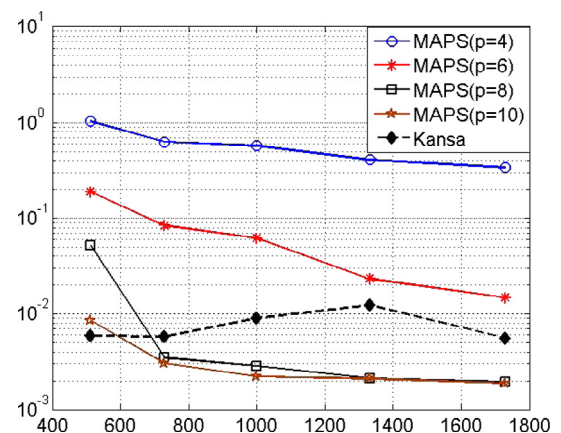


Fig. 2. Example 1. Maximum difference between steady-state solutions and numerical solutions for different numbers of basis by using the present MAPS with $p = 4, 6, 8, 10$ and the Kansa method with MQ RBF.

Table 2
Example 1. Numerical results obtained with $p = 8$ and different temporal parameters.

τ	250	500	750	1000
T	9250	11000	12,750	14,000
T/τ	37	22	17	14
L^∞ difference	5.37E-03	2.85E-03	1.63E-03	1.29E-03
Time (s)	32.0	19.5	15.4	13.2

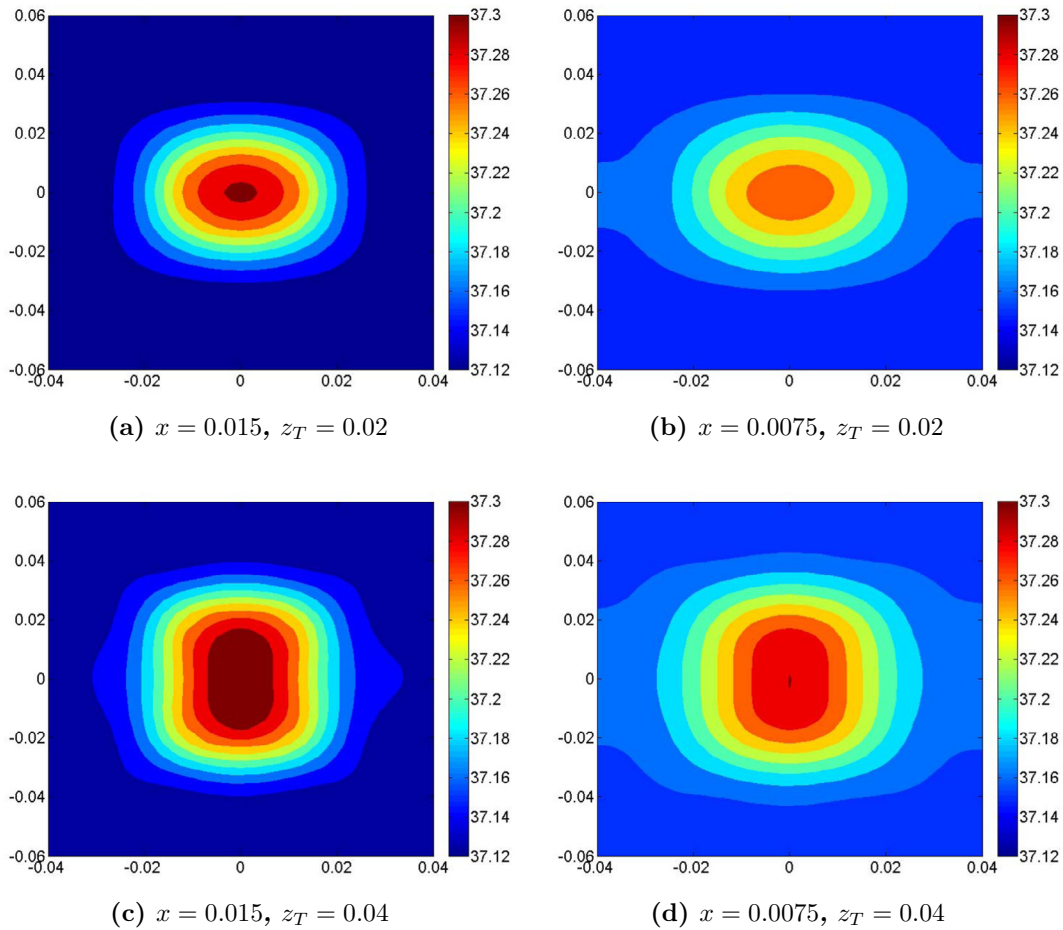


Fig. 3. Example 2. 3D numerical simulated temperature distributions for various tumor widths z_T on some yz -slices at the center of the tumor ($x = 0.015$) and in-between the skin and tumor ($x = 0.0075$).

$$\Omega_T = [0.01, 0.02] \times [-0.01, 0.01] \times [-z_T/2, z_T/2] \text{ for } z_T \in \{0.02, 0.04\}.$$

In any two-dimensional model, assumptions on temperature along certain directions is unavoidable. Since the depth of the tumor beneath the skin has great implication to the complication of the corresponding removal surgery, suppose that one still decides to “discard” the depth in the x -direction. Using our 3D simulations, see Fig. 3, we show the temperature profiles at two depth below the skin: right at the center of the tumor ($x = 0.015$) and in-between the skin and tumor ($x = 0.0075$). Comparing the results for the same z_T but different x , it can be expected that 2D simulations and observed skin temperature are rather different.

In [28], we can find a two-dimensional model that keep the depth but “discard” the z -direction to simulate the cross-section of the tumor. That is, the simulated result is independent of our choice of z_T . In Fig. 4(a) and (b), 2D results are obtained by using the present MAPS and the RBF-MFS method in the literature [28], respectively. We can find that the MAPS results agree well with the RBF-MFS results in the health skin tissue region, and the RBF-MFS results become non-smooth around the tumor region due to introducing error in the interface conditions by using the direct solution of the RBF-MFS matrix. Then in order to make a comparison between 2D and 3D results, we consider two values of z_T in 3D simulation again. Fig. 4(c)–(f) shows ours 3D numerical results restricted to $z = 0$ and $z = -0.025$, i.e., cross-sections at the center and at an off-center position of the tumor, which cannot be capture by the 2D model. We can find that the 2D results agree somewhat with the present 3D results at the ($z = 0$) center of the

tumor. When $z_T = 0.02$, i.e., a square-shaped tumor, we see a less agreement between the 2D and 3D results.

3.3. Example 3. Effect of the tumor geometries

Real tumors are not rectangular. This example investigates the effect of the tumor geometries to the thermal behaviors of the skin tissue. We consider five different geometries¹ with the identical volume. To show that our proposed method can deal with irregular data point density, we use regular data in the parameter space, which yield non-uniformly data points in the tumor domain. See

¹ Geometry 1: $\Omega_T = \{(x, y, z)\}$ defined in spherical coordinates with the geometry centre $(0.015, 0, 0)$ [30] by $R(\psi, \varphi) = r_1(1 + \frac{1}{6} \sin 7\psi \sin 6\varphi)$ for $0 \leq \varphi \leq 2\pi, 0 \leq \psi \leq \pi$ and $r_1 = 0.01$.

Geometry 2: $\Omega_T = [0.01, 0.02] \times [-r_2, r_2] \times [-r_2, r_2]$ with $r_2 = 0.010, 411, 042, 633, 749$.

Geometry 3: Ω_T defined implicitly [31] via the following parametric equation and constant $r_3 = 0.006047253$,

$$\frac{(x + 0.3 \cos(\pi z/r_3) - 0.015)^2}{0.64(1 - 0.4 \cos(\pi z/r_3))} + \frac{y^2}{0.64(1 - 0.1 \cos(\pi z/r_3))} + z^2 \leq r_3^2.$$

Geometry 4: $\Omega_T = \{(x, y, z) : (x - 0.015)^2 + y^2 + z^2/16 \leq r_4^2\}$ with $r_4 = 0.006372354776612$.

Geometry 5: $\Omega_T = \{(x, y, z) : (x - 0.015)^2 + y^2 - z^2/16 \leq r_5^2, |z| \leq 2r_5\}$ with $r_5 = 0.005287949073655$.

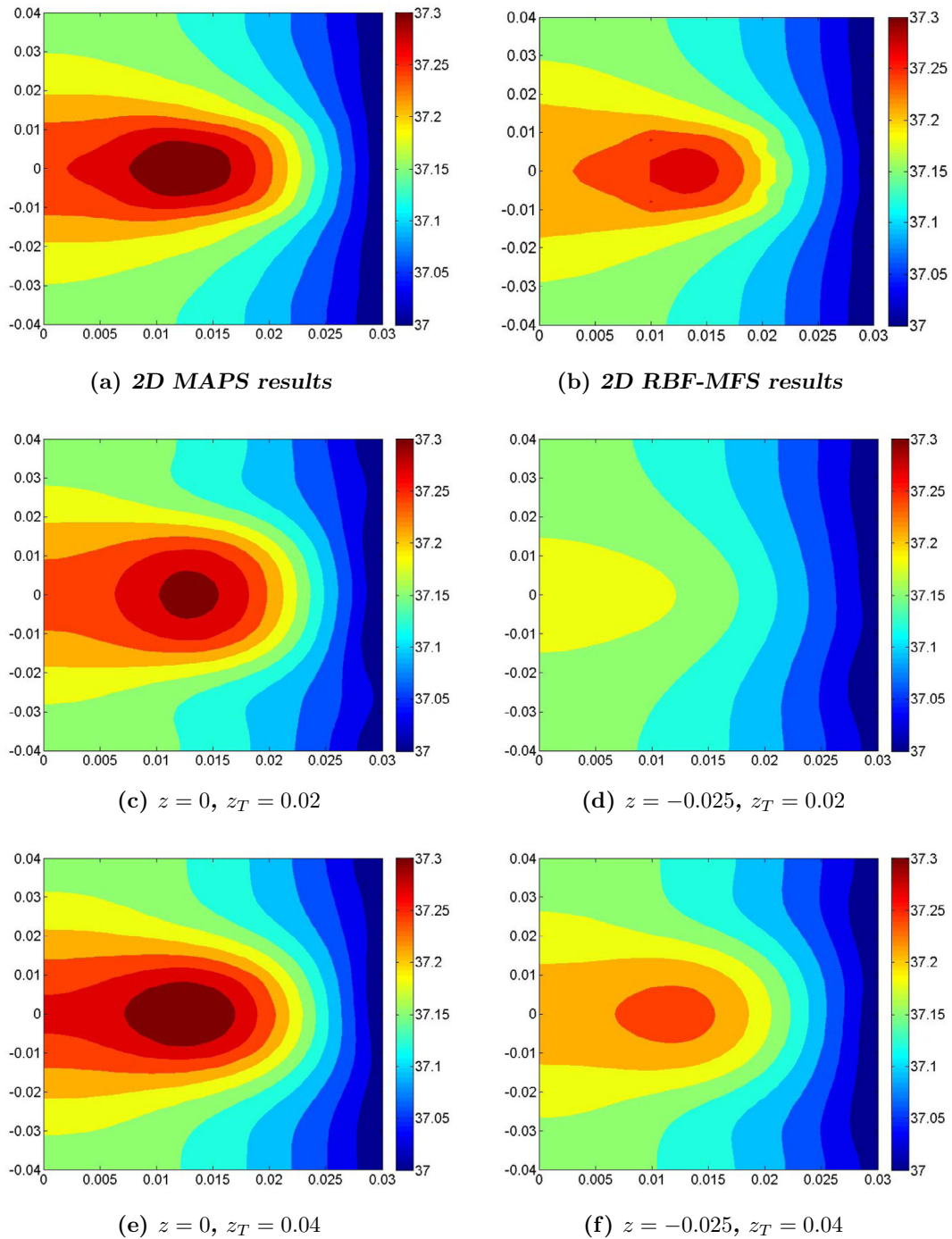


Fig. 4. Example 2. Comparison of 2D and 3D simulated temperature distributions.

Fig. 5 for some schematic demonstrations of data point distributions on the tested geometries.

Fig. 6 depicts numerical results along with the x -axis by using the present 3D model with different tumor geometries. Fig. 7 represents our numerical results along with y -axis by using the present 3D model with different tumor geometries. It can be observed from Fig. 6 that the hyperboloid tumor (Geometry 5) has the different thermal behaviors with the other geometry-shaped tumors along the perpendicular direction to the skin surface, and the tumor-like tumor (Geometry 1) and the rectangular tumor (Geometry 2) almost have the same thermal behaviors along the perpendicular

direction to the skin surface. It can be seen from Fig. 7 different tumor geometries lead to the distinct thermal behaviors of the skin tissue, particularly, in between the tenuous tumors (Geometry 4 and 5) and the rectangular tumor (Geometry 2). Whereas, the asymmetrical tumors (Geometry 1 and 3) produce the tumor-directional thermal behaviors along with y -axis.

3.4. Example 4. Effect of the tumor location

This example investigates the effects of the tumor locations on the thermal behaviors of the skin tissue. We consider four stages of

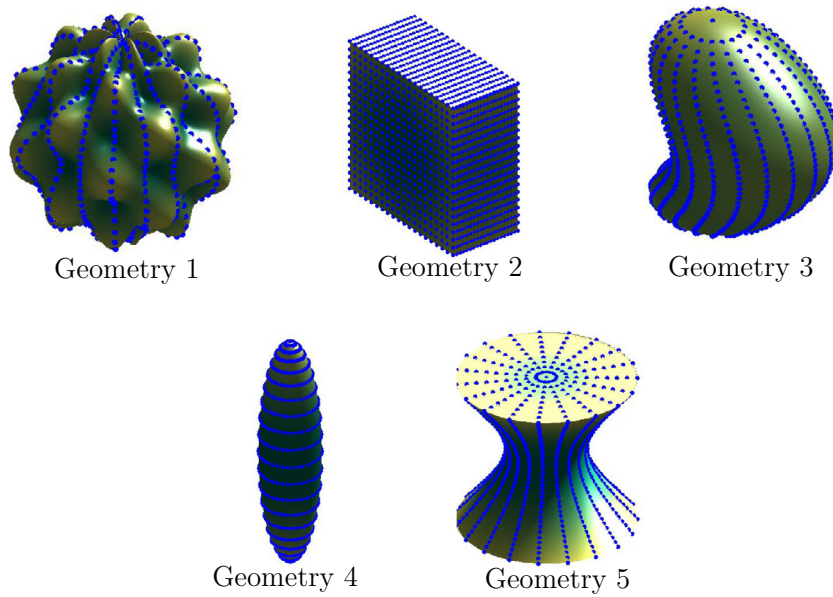
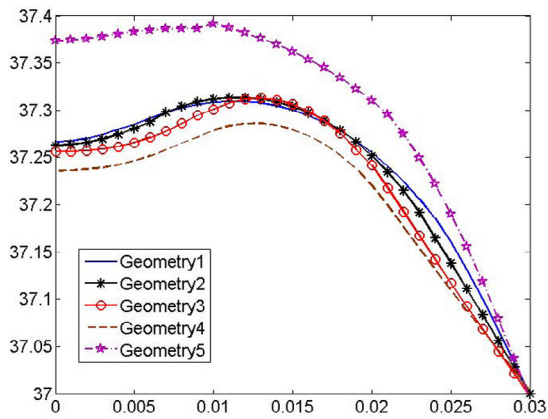
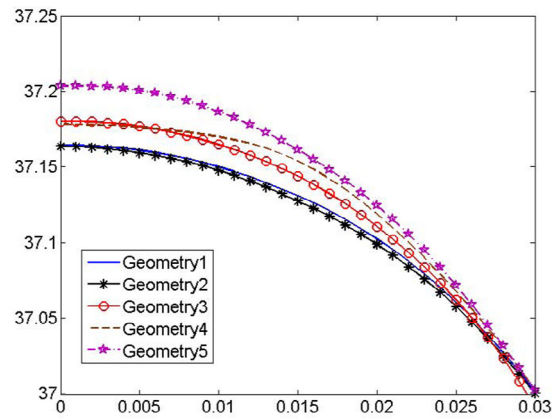


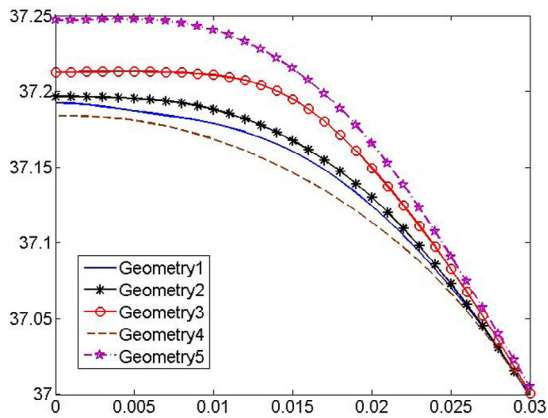
Fig. 5. Configurations of five different tumor geometries in Example 3.



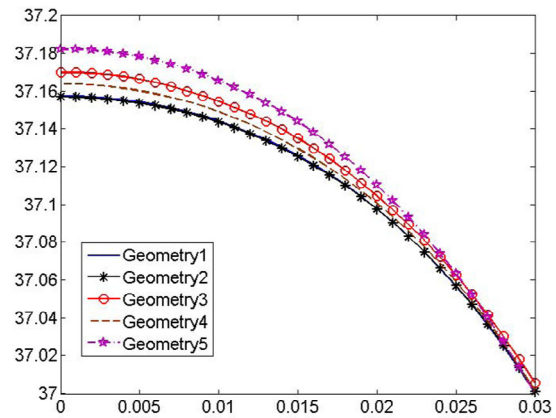
(a) $u(x, 0, 0, T)$



(b) $u(x, 0, -0.03, T)$



(c) $u(x, -0.03, 0, T)$



(d) $u(x, -0.03, -0.03, T)$

Fig. 6. Numerical results along with x axis by using the present 3D model with different tumor geometries in Example 3.

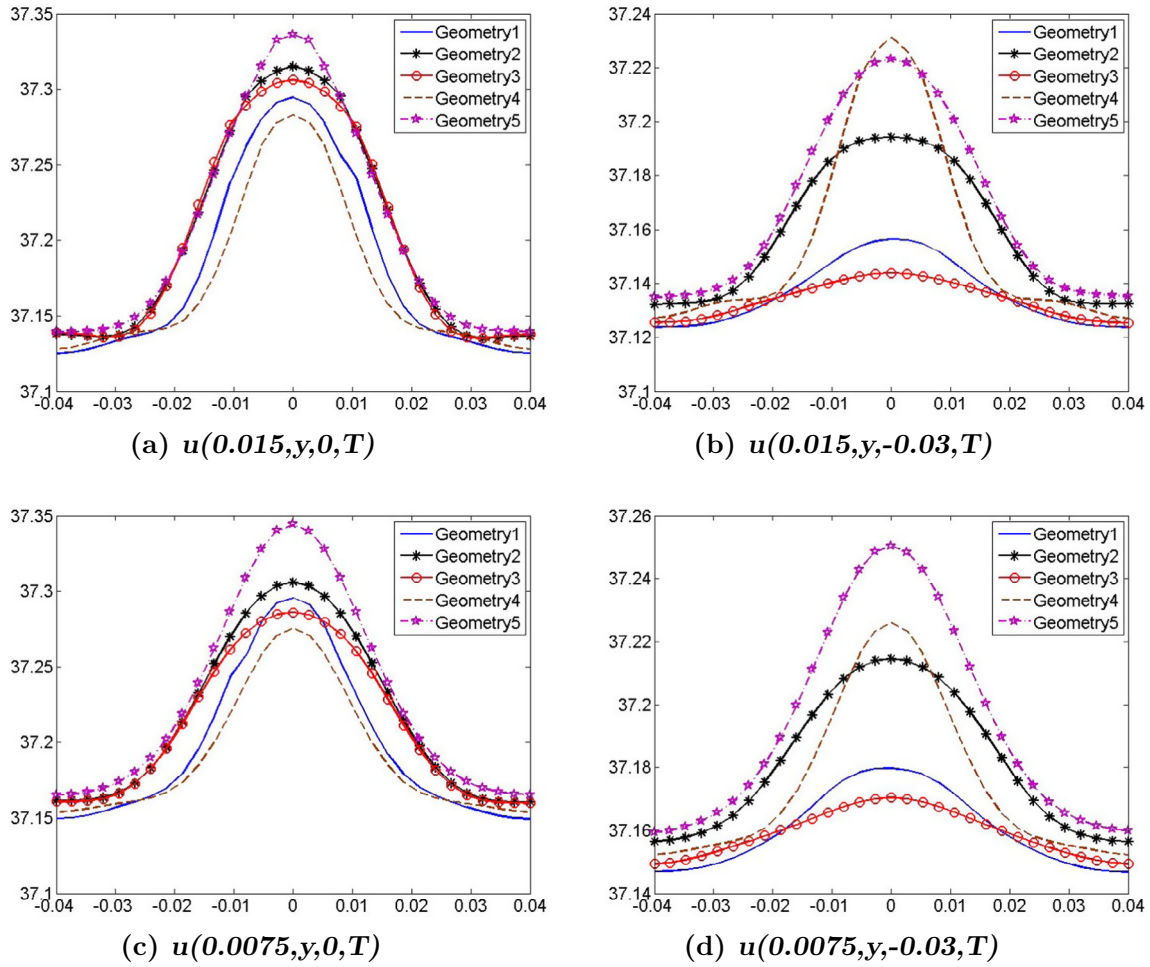


Fig. 7. Numerical results along with y axis by using the present 3D model with different tumor geometries in Example 3.

the tumor² with the same volume. Fig. 8 shows the temperature profiles resulting from these four stages. Fig. 9 shows numerical results by using the present 3D model with different tumor locations. It can be observed that the highest temperature appears inside the tumor region or its nearby regions. The stages 1–3 yields similar results, and its temperature distribution tends to gentle from stage 1 to stage 3. However, two well separated small tumors as in stage 4 has a relatively small thermal effect to skin temperature in comparison to the temperature profiles of stages 1–3.

Finally, it should be mentioned that all the numerical simulation in this paper can be done in three minutes via a laptop (Inter Core i5-4200 M 2.50 GHz, 4.00 GB RAM).

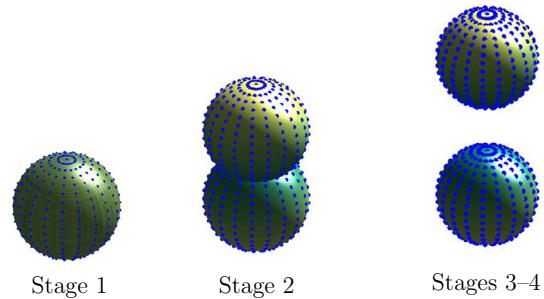


Fig. 8. Configurations of four stages of tumor locations in Example 4.

4. Conclusions

This paper applies the method of approximate particular solutions (MAPS) to investigate the effect of the arbitrary-shaped tumor on the thermal behavior inside 3D skin tissue. To improve the numerical stability of the employed meshless method, an affine space decomposition technique has been adopted also. The present numerical experiments verify that such a combination yields an easy to implement numerical method that is a competitive alternative for solving the 3D Pennes bioheat equation. The method also provides satisfactory simulations under a variety of tumors' geometries, i.e., different locations, shapes, and sizes. The tenuous tumors, i.e., ellipsoid and hyperboloid, give very distinct thermal

² Stage1 Single sphere $\Omega_T = \{(x, y, z) : (x - 0.015)^2 + y^2 + z^2 \leq R_1^2\}$ with where $R_1 = 0.008$.

Stage2 Connected spheres $\Omega_T = \{(x, y, z) : (x - 0.015)^2 + y^2 + (|z| - 0.075R_2)^2 \leq R_2^2\}$ $R_2 = 0.006443237571121$.

Stage3 Nearby spheres $\Omega_T = \{(x, y, z) : (x - 0.015)^2 + y^2 + (z - Lz_1)^2 \leq R_3^2, (x - 0.015)^2 + y^2 + (z + Lz_1)^2 \leq R_3^2\}$ with $R_3 = 0.006349597325461$ and $Lz_1 = 0.01$.

Stage4 Well separated spheres $\Omega_T = \{(x, y, z) : (x - 0.015)^2 + y^2 + (z - Lz_2)^2 \leq R_3^2, (x - 0.015)^2 + y^2 + (z + Lz_2)^2 \leq R_3^2\}$ with $R_3 = 0.006349597325461$ and $Lz_2 = 0.02$.

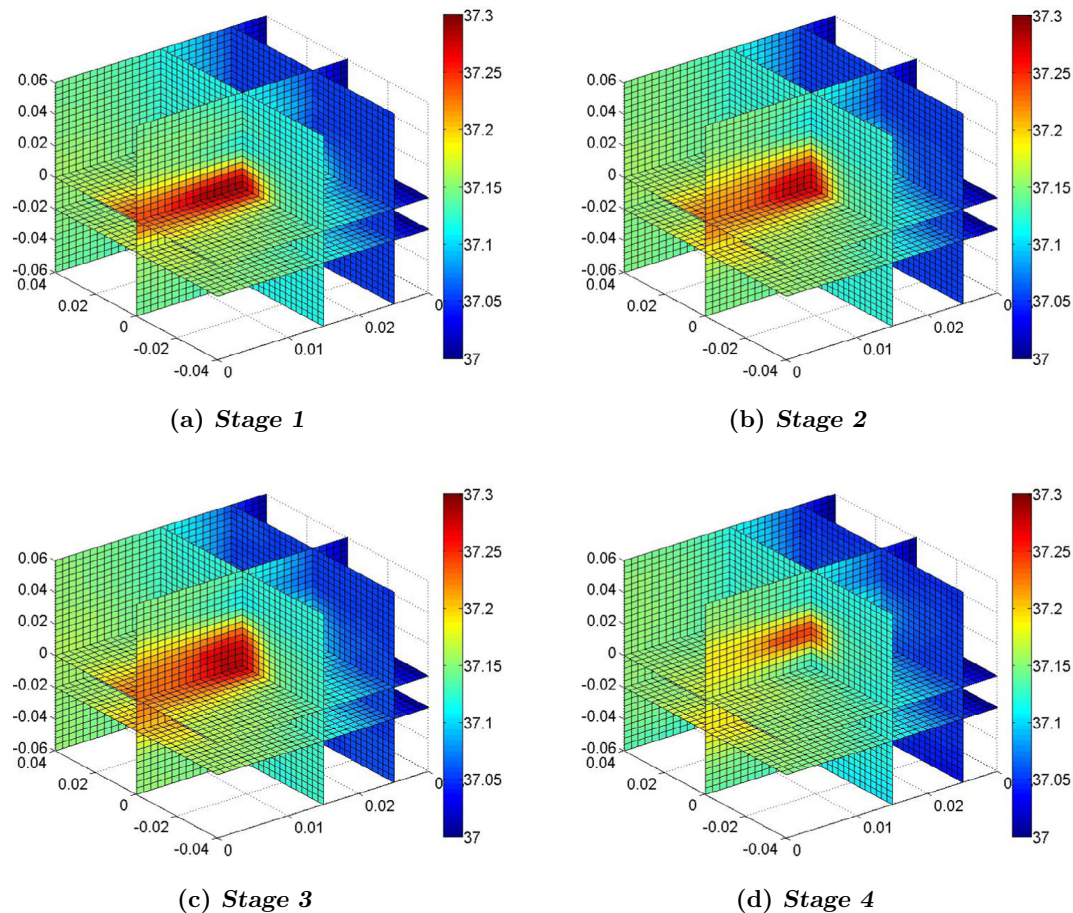


Fig. 9. Numerical results along with x axis by using the present 3D model with different tumor locations in Example 4.

behaviors of the skin tissue in comparison to the ones resulting from rectangular tumors. Moreover, asymmetrical tumors, i.e., tumor-like bumpy sphere and bean shaped, produce directional thermal behaviors parallel to the skin surface. Our simulation also verifies that well separated tumors are harder to detect due to the relative minor changes in skin temperature.

Acknowledgements

The work described in this paper was supported by the National Science Funds of China (Grant Nos. 11302069 and 11372097), the Chinese Postdoctoral Science Foundation (Grant Nos. 2014M561565 and 2015T80492), and the Foundation for Open Project of the State Key Laboratory of Acoustics (Grant No. SKLA201509), the Foundation for Open Project of the Key Laboratory of Road Construction Technology and Equipment, Ministry of Education (Grant No. 310825151132), the Fundamental Research Funds for the Central Universities (Grant No. 2016B06214), the 111 Project (Grant No. B12032), Qing Lan Project, a CERG Grant of the Hong Kong Research Grant Council, and a FRG Grant of HKBU.

References

- [1] J. Liu, L. Xu, Boundary information based diagnostics on the thermal states of biological bodies, *Int. J. Heat Mass Transfer* 43 (16) (2000) 2827–2839.
- [2] E. Ng, N. Sudharsan, Numerical computation as a tool to aid thermographic interpretation, *J. Med. Eng. Technol.* 25 (2) (2001) 53–60.
- [3] K. Das, S. Mishra, Non-invasive estimation of size and location of a tumor in a human breast using a curve fitting technique, *Int. Commun. Heat Mass Transfer* 56 (2014) 63–70.
- [4] H. Pennes, Analysis of tissue and arterial blood temperatures in the resting human forearm, *J. Appl. Physiol.* 1 (2) (1948) 93–122.
- [5] L. Bedin, F. Bazan, On the 2D bioheat equation with convective boundary conditions and its numerical realization via a highly accurate approach, *Appl. Math. Comput.* 236 (2014) 422–436.
- [6] M. Dehghan, M. Sabouri, A spectral element method for solving the pennes bioheat transfer equation by using triangular and quadrilateral elements, *Appl. Math. Model.* 36 (12) (2012) 6031–6049.
- [7] M. Jamil, E. Ng, Evaluation of meshless radial basis collocation method (RBCM) for heterogeneous conduction and simulation of temperature inside the biological tissues, *Int. J. Therm. Sci.* 68 (2013) 42–52.
- [8] C. Chen, C. Fan, P. Wen, The method of approximate particular solutions for solving elliptic problems with variable coefficients, *Int. J. Comput. Meth.* 8 (03) (2011) 545–559.
- [9] C. Chen, C. Fan, P. Wen, The method of approximate particular solutions for solving certain partial differential equations, *Numer. Meth. Part. Diff. Eq.* 28 (2) (2012) 506–522.
- [10] L. Ling, Y. Hon, Improved numerical solver for Kansa's method based on affine space decomposition, *Eng. Anal. Bound. Elem.* 29 (12) (2005) 1077–1085.
- [11] H. Zhu, The method of approximate particular solutions for solving anisotropic elliptic problems, *Eng. Anal. Bound. Elem.* 40 (2014) 123–127.
- [12] M. Li, W. Chen, C. Tsai, A regularization method for the approximate particular solution of nonhomogeneous cauchy problems of elliptic partial differential equations with variable coefficients, *Eng. Anal. Bound. Elem.* 36 (3) (2012) 274–280.
- [13] L. Kuo, M. Gu, D. Young, C. Lin, Domain Type Kernel-Based Meshless Methods for Solving Wave Equations, *CMC: Computers, Materials, & Continua*.
- [14] C. Bustamante, H. Power, W. Florez, C. Hang, The global approximate particular solution meshless method for two-dimensional linear elasticity problems, *Int. J. Comput. Math.* 90 (5) (2013) 978–993.
- [15] C. Fan, C. Yang, W. Lai, Numerical solutions of two-dimensional flow fields by using the localized method of approximate particular solutions, *Eng. Anal. Bound. Elem.* 57 (2015) 47–57.
- [16] C. Bustamante, H. Power, W. Florez, An efficient accurate local method of approximate particular solutions for solving convection-diffusion problems, *Eng. Anal. Bound. Elem.* 47 (2014) 32–37.
- [17] Z. Fu, W. Chen, L. Ling, Method of approximate particular solutions for constant-and variable-order fractional diffusion models, *Eng. Anal. Bound. Elem.* 57 (2015) 37–46.

- [18] E. Kansa, Multiquadrics—a scattered data approximation scheme with applications to computational fluid-dynamics—II solutions to parabolic, hyperbolic and elliptic partial differential equations, *Comput. Math. Appl.* 19 (8) (1990) 147–161.
- [19] E. Kansa, Multiquadrics—a scattered data approximation scheme with applications to computational fluid-dynamics—I surface approximations and partial derivative estimates, *Comput. Math. Appl.* 19 (8) (1990) 127–145.
- [20] G. Yao, S. ul Islam, B. Šarler, Assessment of global and local meshless methods based on collocation with radial basis functions for parabolic partial differential equations in three dimensions, *Eng. Anal. Bound. Elem.* 36 (11) (2012) 1640–1648.
- [21] C. Bustamante, H. Power, W. Florez, A global meshless collocation particular solution method for solving the two-dimensional Navier–Stokes system of equations, *Comput. Math. Appl.* 65 (12) (2013) 1939–1955.
- [22] M. Dehghan, F. Fakhar-Izadi, The spectral collocation method with three different bases for solving a nonlinear partial differential equation arising in modeling of nonlinear waves, *Math. Comput. Modell.* 53 (9–10) (2011) 1865–1877.
- [23] A. Shokri, M. Dehghan, Meshless method using radial basis functions for the numerical solution of two-dimensional complex ginzburg-landau equation, *Comput. Model. Eng. Sci.* 84 (4) (2012) 333–358.
- [24] M. Dehghan, M. Abbaszadeh, A. Mohebbi, A meshless technique based on the local radial basis functions collocation method for solving parabolic-parabolic Patlak-Keller-Segel chemotaxis model, *Eng. Anal. Bound. Elem.* 56 (2015) 129–144.
- [25] W. Chen, Z. Fu, C. Chen, *Recent Advances in Radial Basis Function Collocation Methods*, Springer, 2014.
- [26] L. Ling, R. Opfer, R. Schaback, Results on meshless collocation techniques, *Eng. Anal. Bound. Elem.* 30 (4) (2006) 247–253.
- [27] H. Hu, J. Chen, W. Hu, Weighted radial basis collocation method for boundary value problems, *Int. J. Numer. Meth. Eng.* 69 (13) (2007) 2736–2757.
- [28] L. Cao, Q. Qin, N. Zhao, An RBF–MFS model for analysing thermal behaviour of skin tissues, *Int. J. Heat Mass Transfer* 53 (7) (2010) 1298–1307.
- [29] H. Carslaw, J. Jaeger, *Conduction of Heat in Solids*, second ed., Oxford University Press, 1986.
- [30] A. Lamichhane, C. Chen, The closed-form particular solutions for laplace and biharmonic operators using a gaussian function, *Appl. Math. Lett.* 46 (2015) 50–56.
- [31] Z. Fu, W. Chen, Y. Gu, Burton–Miller–type singular boundary method for acoustic radiation and scattering, *J. Sound Vib.* 333 (16) (2014) 3776–3793.